Heterodox transients in time-domain induced polarization

Fiandaca, Gianluca; Olsson, Per-Ivar; Maurya, Pradip Kumar; Kühl, Anders; Bording, Thue; Dahlin, Torleif; Auken, Esben

Published in:
Geophysics

DOI:
10.1190/geo2020-0808.1

2022

Document Version:
Publisher's PDF, also known as Version of record

GEOPHYSICS, VOL. 87, NO. 1 (JANUARY-FEBRUARY 2022); P. E35–E47, 14 FIGS., 2 TABLES.
10.1190/GEO2020-0808.1

Heterodox transients in time-domain-induced polarization

Gianluca Fiandaca[1], Per-Ivar Olsson[2], Pradip Kumar Maurya[3], Anders Kühl[3], Thue Bording[3], Torleif Dahlin[2], and Esben Auken[4]

ABSTRACT

Negative-induced polarization (IP) time-domain transients, sign-changing or nonmonotonically decaying transients, are currently often considered as measurement errors and are removed in data processing. These transients, here called heterodox in the sense of other than generally accepted signals, might originate from measurement errors, inductive effects, or poor signal processing, but synthetic modeling and field measurements indicate that these transients are physically possible. A simple theoretical explanation of the basic mechanism for their origin can be found through the superposition of contributions from regions with different sensitivities, and such heterodox transients can be identified through the processing of full-waveform IP data. A mathematical classification of orthodox and heterodox IP transients into six different types is evaluated based on the temporal development of the sign of their amplitude and derivative. The basic mechanism for IP transients with heterodox shapes is further investigated by considering the subsurface Cole-Cole parameter sensitivities and time-varying IP potential for 2D synthetic models. The time-domain forward response and sensitivities are computed through a time transformation that accounts for the current waveform. This approach allows for quantitative unbiased estimates of the time-domain transients and sensitivities, different from the estimates obtained when using multiple direct-current forward computations, as is often done in the inversion of time-domain IP data. Time-domain IP transients may differ from the traditionally expected decaying-like transients when the electrode geometry has IP potential sensitivities with different signs for areas with different IP parameters. Hence, previously disregarded IP transients containing valuable information of the subsurface can be kept for inversion and contribute to the final parameter distribution. An increased understanding of theoretically possible IP transients makes way for more accurate processing of data in the future, reducing the time and resources needed for spectral inversion of time-domain data.

INTRODUCTION

The research community in the time-domain-induced polarization (IP) method has recently moved from evaluating only the transient IP responses as integral chargeability considering the mean value of the transients to also considering the spectral information contained in the shape of the IP transients (Hördt et al., 2006; Hönig and Tezkan, 2007; Fiandaca et al., 2012, 2013; Madsen et al., 2017; Kang and Oldenburg, 2018). This change in evaluation has enabled the extraction of spectral IP parameters from time-domain field acquisitions, for instance, for characterization of landfills and contaminated sites (Gazoty et al., 2012a; Johansson et al., 2015; Wemegah et al., 2017), for geologic discrimination (Gazoty et al., 2012b; Johansson et al., 2017; Rossi et al., 2017), for permeability estimation (Fiandaca et al., 2018; Maurya et al., 2018), for time-lapse monitoring of CO_2 injection (Doetsch et al., 2015a; Fiandaca et al., 2015), and active layer thickness in permafrost applications (Doetsch et al., 2015b). Furthermore, recent developments in signal processing of full-waveform data from time-domain IP measurements, comprising harmonic denoising and improved background removal, have enabled retrieval of early-time IP information as well as accurate retrieval of late times (Olsson et al., 2016). This increased attention to the full IP transients has

Manuscript received by the Editor 10 November 2020; revised manuscript received 22 April 2021; published ahead of production 4 October 2021; published online 18 November 2021.
[1]University of Milano, Department of Earth Sciences "Ardito Desio," Milano IT-20122, Lombardia, Italy. E-mail: gianluca.fiandaca@unimi.it.
[2]Lund University, Engineering Geology, Lund Box 117, SE-221 00, Sweden. E-mail: per-ivar.olsson@tg.lth.se (corresponding author); torleif.dahlin@tg.lth.se.
[3]Aarhus University, HydroGeophysics Group, Department of Geoscience, Aarhus DK-8000, Denmark. E-mail: pradip.maurya@geo.au.dk; anders.kuhl@geo.au.dk; bording@geo.au.dk.
[4]Geological Survey of Denmark and Greenland, Kobenhavn DK-1350, Denmark. E-mail: ea@geus.dk.

DOI:10.1190/geo2020-0808.1

increased the demands on data quality and accuracy as well as processing and removal of erroneous data before geophysical inversion. It has been known for decades that negative apparent integral IP transients (negative mean value) can represent correct measurements of the subsurface potential transients (Bertin and Loeb, 1976; Loeb and Bertin, 1976; Sumner, 1976; Yuval and Oldenburg, 1997), but it appears that this has not attracted the required attention and such data have therefore been discarded by practitioners and often by researchers as well. Dahlin and Loke (2015) bring attention to this, explaining that it depends on how the chargeable zones are geometrically distributed in the ground in relation to the sensitivity function of the electrode configuration. They also demonstrate that the resolution of the inverted model can be severely affected if the negative IP data are discarded. For frequency-domain measurements, corresponding explanations for positive apparent phase values have been suggested, including reasoning based on analogous electrical circuits (Wang et al., 2021), and inversion algorithms capable of handling such data (Kemna, 2000). For time-domain measurements, the reported IP transients are typically strictly positive monotonic functions trending to zero, denoted *orthodox* in this paper for brevity, in the sense of considered acceptable by most practitioners and researchers. However, heterodox shapes have also been described as physically possible in the literature, e.g., by Yuval and Oldenburg (1997); nevertheless, such IP transients are often regarded as measurement errors as well and are not routinely recognized as acceptable signals within the IP community. This is because heterodox transients might originate by unproper background removal, erroneous instrumental or measurement behavior, or early-time electromagnetic effects. Hence, the objectives of this study have been to make use of recent measurement and processing routines for full-waveform data, to allow for discriminating correct IP signals from erroneous data, and to open up for proper use of heterodox IP transients in data inversion.

This paper also presents a deeper inspection of the background removal procedure described in Olsson et al. (2016) and suggests an additional procedure for reducing the risk of interpreting erroneous transients as actual IP effects. Furthermore, we give an explanation of the origin of heterodox transients by illustrating the sensitivity pattern for specific electrode configurations and geometric distributions of the IP parameters, and we show the differences with the approach used by Dahlin and Loke (2015) as well as with approaches that invert the IP gates independently with direct-current (DC) algorithms (Hördt et al., 2006; Hönig and Tezkan, 2007).

Our paper is organized as follows. We start by introducing data from field measurements from Grindsted (Denmark) where approximately 50% of the IP transients are negative or have other heterodox shapes. Following this, we suggest a classification of IP transient types, show examples of heterodox signals due to improper background removal and erroneous measurements, and we suggest ways of filtering out erroneous heterodox transients. Subsequently, we revise the different approaches in IP modeling, and we explain the basic mechanism behind IP transients with heterodox shapes with examples of synthetic models that generate such transients. Finally, we show an inversion model for the field measurements, which reproduces the positive and negative, as well as the heterodox IP transients.

FIELD DATA AND IP TRANSIENT CLASSIFICATION

Time-domain resistivity and IP measurements were performed along a 600 m profile at a landfill site in Grindsted, Denmark, in November 2014. The profile was collected using 121 acid-grade stainless steel electrode rods spaced at approximately 5 m, but the electrode at the profile coordinate 325 m was excluded from the measurements because of poor contact. The instrument ABEM Terrameter LS was used for injecting a 50% duty-cycle current with 4 s pulse length with three stacks with voltage measurements in a total of 1801 multiple gradient array arrangements. The electrode contact resistance was estimated for all electrodes with the focus-one protocol (Ingeman-Nielsen et al., 2016) resulting in a mean electrode contact resistance of 1210 Ω with a standard deviation of 650 Ω. Full-waveform data for transmitted current and received potentials were recorded at 1 kHz and processed according to Olsson et al. (2016) for background removal, despiking, and removal of harmonic noise. IP data were gated starting from 1 ms after the current turn-off, with seven gates per decade and log-increasing gate widths, giving 25 gates per stacked IP transient.

After the full-waveform signal processing, the stacked IP and DC data were carefully examined manually for obvious outliers, identified by the lack of coherence among different DC and IP gate magnitudes in the pseudosections, or within the IP transients themselves. The manual examination resulted in the full removal of 43 quadrupoles (removing the DC and all IP data points), the full IP removal of an additional 137 quadrupoles (removing all IP data but keeping the DC data), and partial filtering of individual IP gates for multiple other quadrupoles. In total, the filtered data set corresponds to 1758 DC data points and 1621 IP transients for further analysis.

The stacked IP transients are divided into six different types based on the temporal development of the sign of their amplitude and their derivative (negative, zero, or positive magnitude and slope), summarized in Figure 1. The types include the standard IP transients with positive amplitude and negative derivative (type positive, P) and five heterodox IP transient types. The heterodox types are made up of a negative (N) IP transient with negative amplitude and positive derivative; a positive-negative (PN) IP transient with PN amplitude and negative derivative (possibly followed by a further change of sign and/or zero and positive derivative); a negative-positive (NP) IP transient with NP amplitude and positive derivative (possibly followed by a further change of sign and/or zero and negative derivative), a zero derivative (ZD) IP transient with an amplitude not passing zero, but with one ZD, and finally, a multiple ZD (MZD) IP transient with amplitude not passing zero, but with MZDs. For estimating the derivative of the IP transients, we are assuming that the derivative of the IP transients is continuous, meaning that the derivative is zero between two data points for which the derivative has different signs. Furthermore, we compute derivatives with a regularized differentiation algorithm (Chartrand, 2011) to prevent small fluctuations in IP amplitude from rendering false indications of ZDs.

Table 1 shows a summary of the field IP transients classified into the six different IP transient types. Approximately 50% of the data are of heterodox IP transient types, dominated by type N and NP followed by ZD, PN, and MZD. Other profiles acquired in the same area presented similar percentages of heterodox transients. Moreover, with 50% of the IP data made of heterodox types, only using the standard type P data would exclude a considerable amount of the available information of the subsurface.

Figure 2 shows the field IP data pseudosections with apparent integral chargeability and the classified IP transient type. There is a distinct zone of negative apparent integral chargeability and IP

transient type N at shallow pseudodepths (28–38 m) from profile coordinates approximately 75–600 m. In connection with this zone, there are clusters with IP transients of type PN and NP as well as the ZD types ZD and MZD. At larger pseudodepths, the apparent integral chargeability is generally positive and of larger magnitude, and the IP types are dominated by type P as a background with a few scattered heterodox types. The colored circles with black outline in Figure 2 mark the pseudopositions, and IP transient types of the exemplifying IP transients are shown in Figure 1.

IDENTIFYING ERRONEOUS HETERODOX TRANSIENTS

An ineffective background removal procedure might, in addition to generating erroneous late IP times, also generate false PN or NP type transients. The aim of the background removal is to cancel effects of telluric self-potentials or current induced electrode polarization (Dahlin et al., 2002), leaving behind a potential signal without background drift. Such an idealized drift-removed signal should regularly alternate at approximately zero, with each pulse possibly being slightly different from the previous ones due to the effect of superposition of all the preceding pulses (Fiandaca et al., 2012). Furthermore, even in the presence of heterodox transients, each pulse transient in the drift-removed signal should tend to equilibrium (for the 50% duty cycle) at late times, when the polarization fades off, given that the acquisition time is sufficiently long compared with the polarization processes at hand. However, note that depending on the IP transient type, the pulse shapes will behave differently and approach zero from the opposite side of the injection current for a type-N transient compared with a type-P or even crossing zero for PN or NP transient types. Following this reasoning, all transients that do not exhibit these properties after background removal can be considered erroneous and should thus be rejected before inversion.

Figure 3 shows the full-waveform potential for two exemplar quadrupoles acquired along the acquisition line, both with large variation in background potential. The Cole-Cole-like background removal fit (Figure 3a and 3d) fits well in both cases with the residuals being fairly evenly distributed around zero (Figure 3b and 3e). However, comparing the development over time for the residuals, the two examples are fundamentally different. Figure 3a–3c shows residuals with alternating slopes, which are approaching zero for all pulses, and it has late-time data alternating around zero after background removal. In contrast, Figure 3d–3f shows disordered residuals with a significant difference in shapes among residual development for the different pulses and also shifts between moving toward and away from the baseline.

As mentioned earlier, regularity in the residual shape is expected for a real IP signal with effective background removal. Therefore, this feature was used to establish a simple filter, which discards heterodox IP transients based on signals with background fit residuals exhibiting such irregularity. In particular, the filter is a binary (accepted or nonaccepted), based on the following three acceptance criteria:

1) The background removal residuals alternate around the baseline for the different pulse signs.
2) The background removal residuals are of the same type, as in our heterodox transient classification.
3) The background removal residuals tend to the baseline.

Figure 4 shows a sketch of full-waveform measurements depicting these three criteria and their fulfillment and failure.

These checks are made for every waveform recording, allowing for identifying erroneous transients originated from either poor background removal (through criteria 1 and 2), as for the transient given by the measurement instrument based on linear background removal (Figure 3c, magenta line) or by erroneous measurements or instrumental behavior (criterion 3) as for the bottom waveform in which the residuals do not always tend to zero after background removal (Figure 3d–3f).

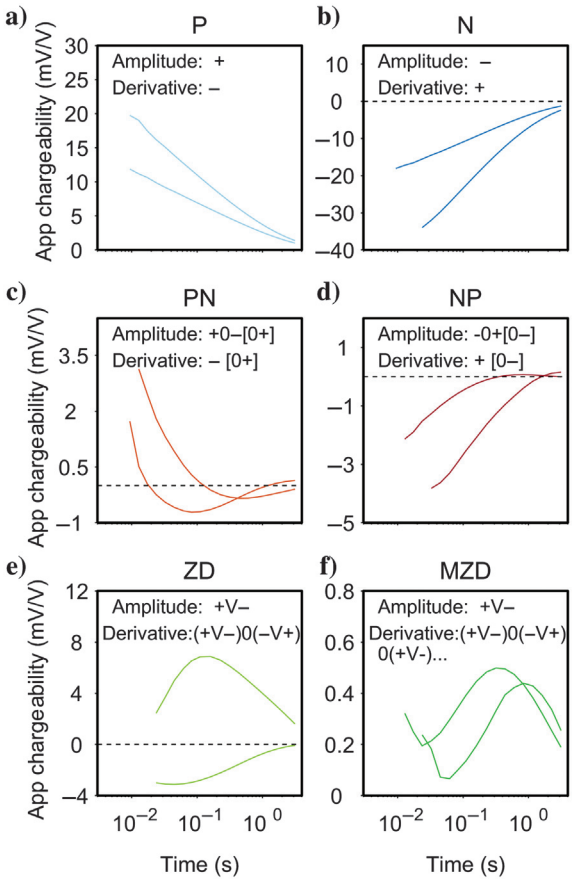

Figure 1. (a-f) Summary of the possible temporal development of amplitude and derivative for the six IP transient types with examples acquired in the field. In the figure, "V" indicates the or-operator, whereas the parenthesis indicates the optional developments. The focus positions of the example transients are marked with circles of corresponding colors in Figures 2a and 2b and 13a and 13b. Note that the transients are plotted in lin-log scale and that the apparent chargeability ranges differ between the panels.

Table 1. Summary of the number of transients in the field data corresponding to each IP transient type.

IP transient type	P	N	PN	NP	ZD	MZD
Number of transients in the field data (—)	858	399	39	202	105	18
Percent of transients in the field data (%)	52.9	24.6	2.4	12.5	6.5	1.1

DIFFERENT APPROACHES FOR MODELING OF IP TRANSIENTS

In the following, we are going to discuss three different approaches for modeling time-domain IP transients: the seminal approach introduced by Seigel (1959); the gate-by-gate approach, in which each IP gate is treated separately by a DC forward modeling (Hördt et al., 2006); and the approach introduced by Fiandaca et al. (2013), in which the full solution of Poisson's equation is considered. The latter approach is compared in detail with the other two approaches, in terms of sensitivity and the modeling results.

Seigel's seminal approach

Dahlin and Loke (2015) present resistivity and chargeability distributions that generate negative IP transients. Their present work is based on Seigel (1959), who develop a mathematical formulation of the IP phenomenon. In particular, in Seigel's approach, the electric field E' and the electric potential Φ' of a polarizable medium are computed through a DC solution of the Poisson's differential equation, substituting the conductivity vector σ, which contains the conductivity values of the model discretization, with the vector $\sigma \cdot (1 - m)$, where m represents the model chargeability. In Seigel (1959), the apparent chargeability m_a, the chargeability in data space measured just after the current turn-off, is then computed as $(\Phi' - \Phi)/\Phi'$, where Φ is the potential of the medium without chargeability, computed with σ.

Following Seigel's approach, the apparent chargeability m_a can also be expressed as

$$m_a = \sum_i m_i \rho_i \frac{\partial \rho_a}{\partial \rho_i} / \rho_a', \qquad (1)$$

where m_i and ρ_i represent the chargeability and resistivity in the model subdivisions and ρ_a'

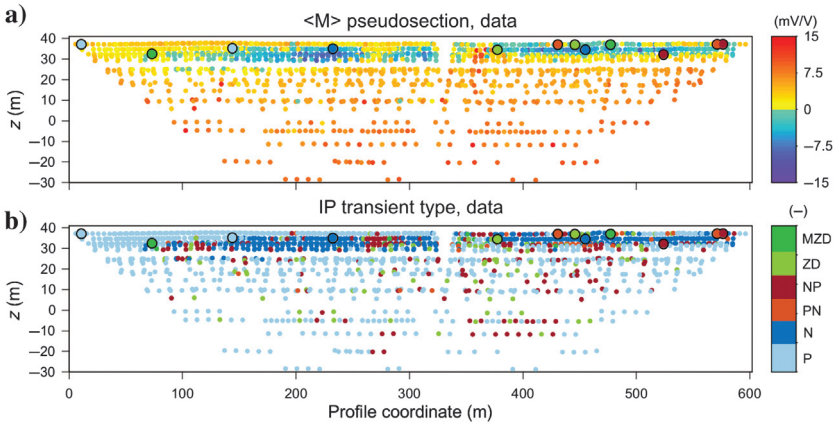

Figure 2. (a) Pseudosections showing the apparent integral chargeability and (b) IP transient type for the field IP data set. The colored circles with a black outline mark the positions and the transient types of the example transients shown in Figure 1.

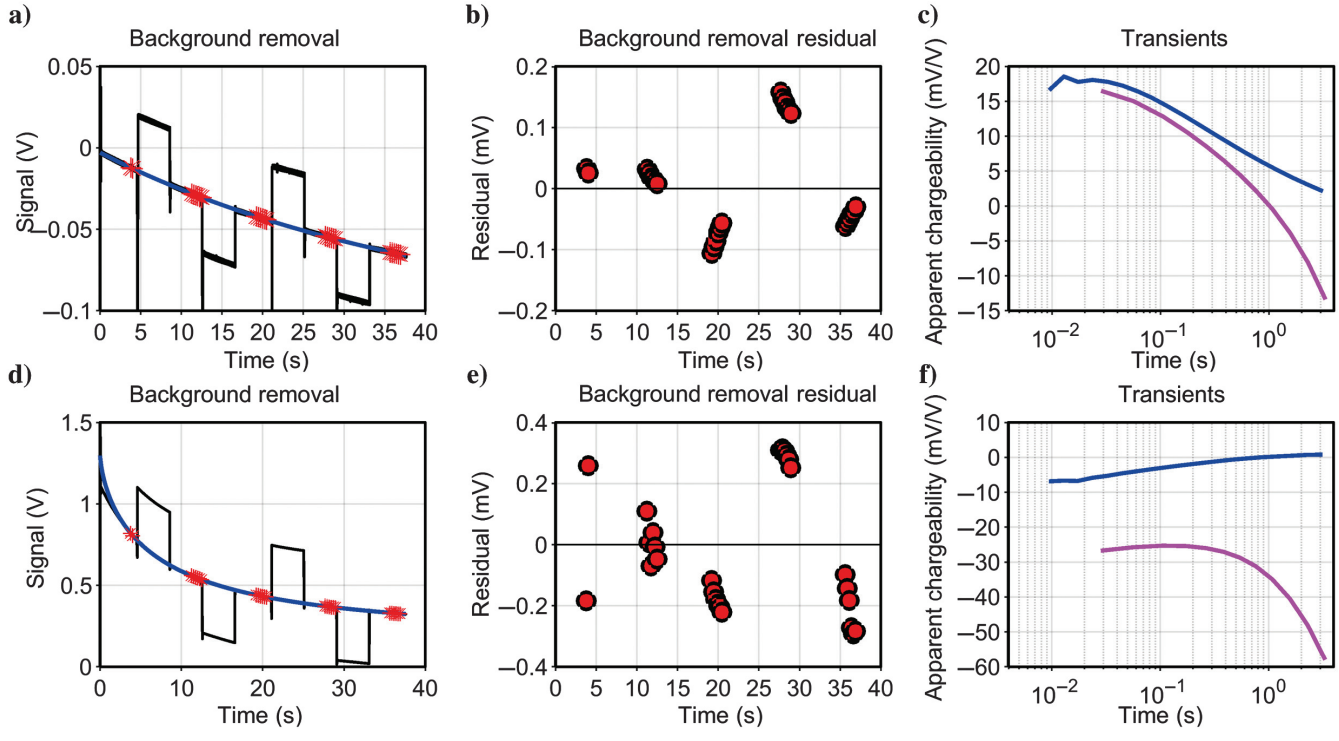

Figure 3. Examples of the background removal for two current quadrupoles (a-c and d-f, respectively). (a and d) Potential signal over time (black) and Cole-Cole-based background removal (blue), and the gated subset used in the background fit (the red stars). (b and e) Residual of the background fit. (c and f) Resulting IP transients (blue) after stacking the transients from the different pulses, together with IP transients supplied directly by the instrument (magenta).

DOI:10.1190/geo2020-0808.1

represents the apparent resistivity inclusive of the polarization effects. When the chargeability is low $\rho_a' \cong \rho_a$ and in equation 1 the apparent chargeability is a homogeneous function of first degree in m (Spiegel, 1974) because $m_a(\alpha \cdot m) = \alpha \cdot m_a(m)$ for any positive constant α. Any homogeneous function of first degree $f(\mathbf{x})$ can be expressed as $f(\mathbf{x}) = \sum_i x_i(\partial f/\partial x_i)$ (Spiegel, 1974), so we can write using the properties of the homogeneous functions and equation 1:

$$\frac{\partial m_a}{\partial m_i} \cong \rho_i \frac{\partial \rho_a}{\partial \rho_i} / \rho_a. \tag{2}$$

Consequently, in Seigel's approach, the sensitivity of the apparent chargeability m_a is derived from the sensitivity of the apparent resistivity ρ_a and the resistivity distribution ρ, but it does not depend on the chargeability distribution m. The apparent resistivity is also a homogeneous function of the first degree in ρ (Seigel, 1959), so that

$$\rho_a = \sum_i \rho_i \frac{\partial \rho_a}{\partial \rho_i}. \tag{3}$$

When the chargeability is low, $\rho_a' \cong \rho_a$, equation 1 can be rewritten as

$$m_a = \sum_i m_i \frac{\partial \log \rho_a}{\partial \log \rho_i} = \sum_i m_i \frac{\partial \log \rho_a}{\partial \log \rho_i} / \sum_i \frac{\partial \log \rho_a}{\partial \log \rho_i}, \tag{4}$$

where the second equality is a direct consequence of equation 3. As long as all the $\partial \log \rho_a/\partial \log \rho_i$ coefficients are positive, the apparent chargeability is a weighted average of the medium chargeability values, comprised within the extreme values of m_i, but whenever some of the $\partial \log \rho_a/\partial \log \rho_i$ coefficients are negative, the m_a value can be outside the m_i range; when the higher m_i values are in the areas of negative sensitivity, the apparent chargeability can be negative, as shown, for instance, by Yuval and Oldenburg (1997) and Dahlin and Loke (2015).

Gate-by-gate approach

Hördt et al. (2006) present another approach for chargeability modeling based on the solution of a DC problem, in which the IP transients are computed independently gate by gate. This approach is based on replacing the convolution of the time-dependent conductivities (with the electric field) by multiplication in Poisson's differential equation. For obtaining negative apparent chargeability values in the gate-by-gate approach, it is necessary to generate negative apparent resistivity values with a DC forward response. Although 3D forward modeling can generate negative apparent resistivity data (Jung et al., 2009), it is in our experience difficult, if not impossible, with 2D modeling.

Full solution of Poisson's equation approach

In this study, we did not follow the approaches proposed by Seigel (1959) or Hördt et al. (2006) for the computation of the Jacobian of apparent chargeability, but the time-domain full-response computation is presented in Fiandaca et al. (2013). Such an approach is comprised of three steps: (1) the Jacobian computation in the frequency domain through the adjoint method, (2) the multiplication with the partial derivative of the complex conductivity versus the IP parameter, and (3) the time transformation, considering the current waveform and, if needed, system filters. No approximations are made with this approach, except for neglecting the EM effects in the frequency-domain solution of the differential equation. The method is fully general and can be applied with any parameterization of the complex resistivity, for instance, the Cole-Cole model (Cole and Cole, 1941; Pelton et al., 1978) and the constant phase angle model (Van Voorhis et al., 1973). In the resistivity form of the Cole-Cole model (Pelton et al., 1978), the complex resistivity is described through four parameters: the DC resistivity ρ_0, the intrinsic chargeability m_0, the relaxation time τ_ρ (the inverse of the angular frequency at which the imaginary part of the complex resistivity has a minimum), and the frequency exponent C. The first two parameters of the Cole-Cole model are similar to Seigel's model parameters, but in the Cole-Cole modeling, the time-domain steady-state condition (meaning the condition reached when the current flows for an infinite time) is an electric potential computed with the distribution of the ρ_0 resistivity values, and not with $\rho_0/(1 - m_0)$ (which would be fully analogous to Seigel's approach). Simply speaking, in the Cole-Cole model, the conduction and the polarization act in parallel.

In this study, the complex resistivity is modeled in terms of the maximum phase angle (MPA) reparameterization of the Cole-Cole model (Fiandaca et al., 2018), in which the intrinsic chargeability

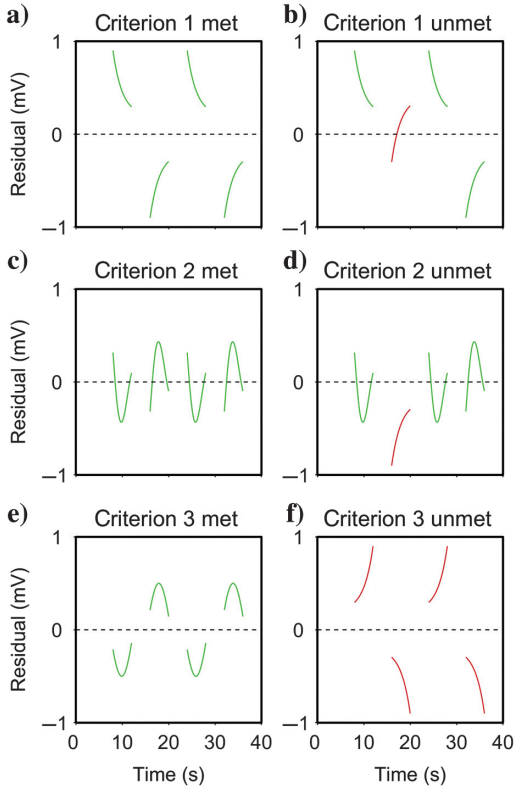

Figure 4. Criteria for rejection of data with incorrect behavior around the background with met criteria in (a, c, and e) and unmet criteria in (b, d, and f). (a and b) Criterion 1, i.e., alternance around the background; (c and d) criterion 2, i.e., pulse types; and (e and f) criterion 3, i.e., late-time tendency.

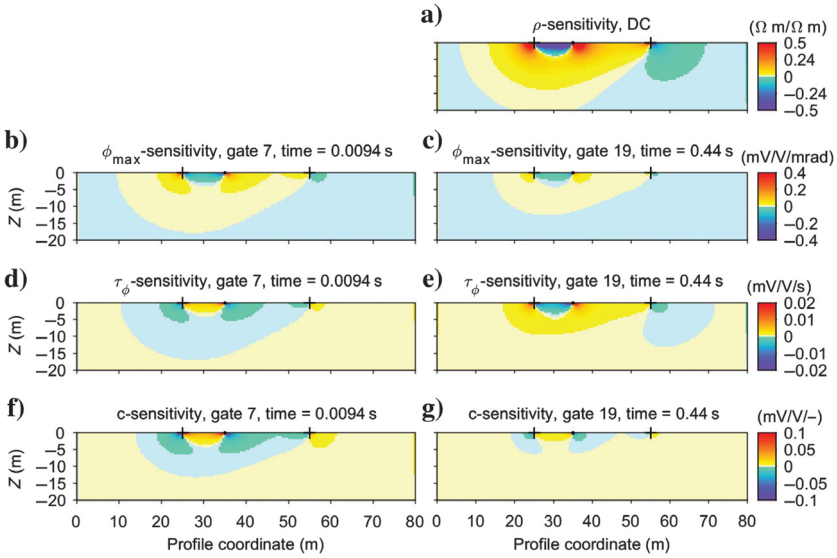

Figure 5. The DC and IP sensitivity distributions for (a) DC and IP data gates (b, d, and f) 7 and (c, e, and g) 19. The sensitivity distributions are calculated for a homogeneous half-space ($\rho = 100$ Ωm, $\varphi_{max} = 5$ mrad, $\tau_\varphi = 0.5$ s, and $C = 0.5$) for a surface quadrupole with $C1 = 25$ m, $C2 = 55$ m, $P1 = 35$ m, and $P2 = 45$ m.

m_0 and the relaxation time τ_ρ are replaced by the maximum phase of the Cole-Cole conductivity φ_{max} and the relaxation time τ_φ (the inverse of the angular frequency at which φ_{max} is reached). This is because φ_{max} and C are less correlated than m_0 and C, resulting in a better parameter resolution with the MPA inversion. Consequently, we can write for each gate of the full-response IP signal

$$m_{a,j} = f_j(\rho_0, \varphi_{max}, \tau_\varphi, C), \qquad (5)$$

where j represents the gate index, $(\rho_0, \varphi_{max}, \tau_\varphi, C)$ are the parameter vectors, defined in all of the model subdivisions, and f_j represents the forward mapping for the jth gate.

Figure 5 shows the sensitivity distribution of the DC datum and two gates (gates 7 and 19) for MPA model parameters for a homogeneous half-space ($\rho_0 = 100$ Ωm, $\varphi_{max} = 5$ mrad, $\tau_\varphi = 0.5$ s, and $C = 0.5$). The same current waveform and gate definition as used in the field data are used in the Jacobian computation. A surface dipole-pole array, with current electrodes placed

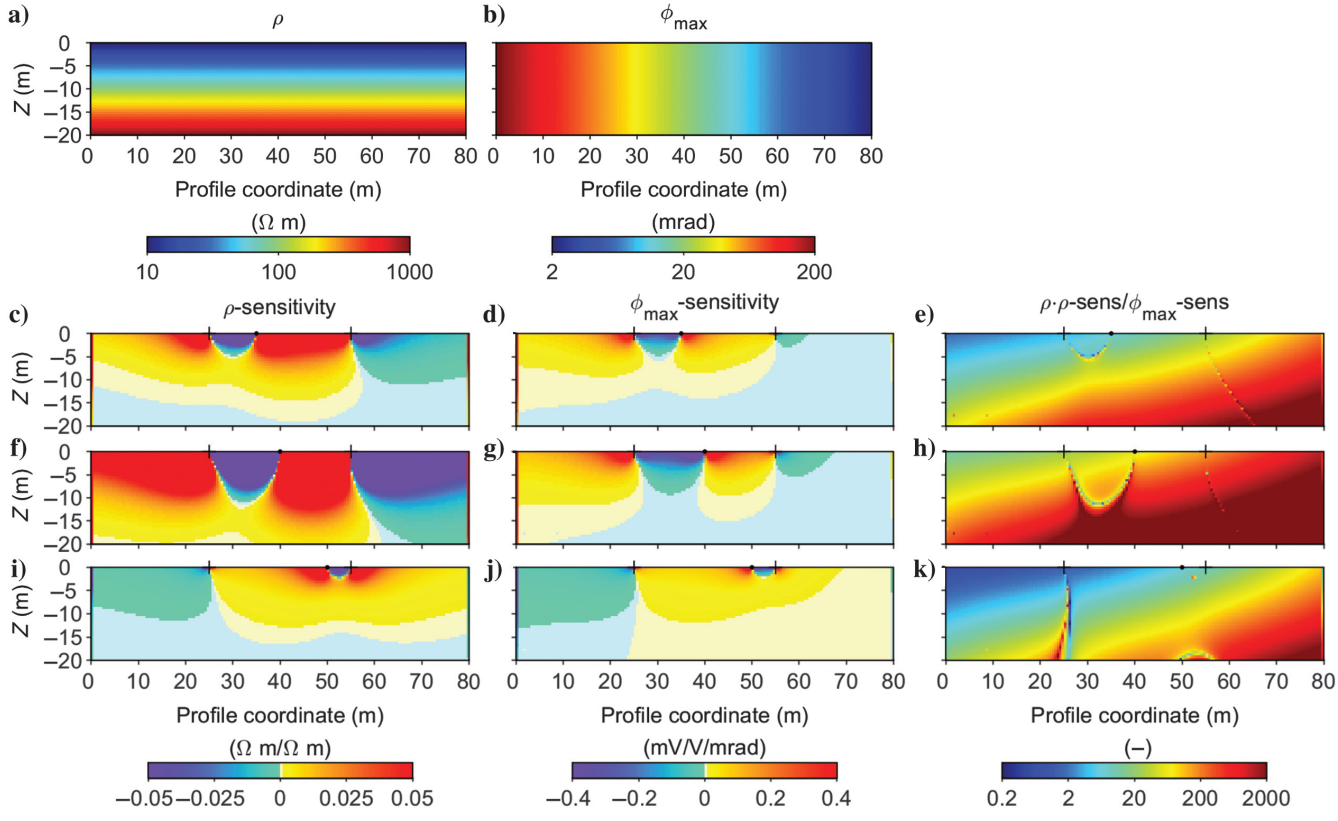

Figure 6. (c, f, and i) The DC ρ-sensitivity, (d, g, and j) the φ_{max}-sensitivity of the seventh gate, and (e, h, and k) the ratio $\rho \cdot \rho$-sensitivity/φ_{max}-sensitivity, that is the chargeability sensitivity of Seigel's approach divided by the φ_{max}-sensitivity of the approach used in this study, together with the (a and b) ρ and φ_{max} model parameters, which vary linearly with the vertical and horizontal dimension, respectively. Three different dipole-pole surface configurations are shown with current dipole (cross markers) $C1 = 25$ m and $C2 = 55$ m and potential electrodes (dot marker) (c-e) $P1 = 35$ m, (f-h) 40 m, and (i-k) 50 m.

at $C1$ = 25 m and $C2$ = 55 m and the potential electrode placed at $P1$ = 35 m, is modeled. The choice of a dipole-pole array for the Jacobian computation was made because with such an array it is possible to easily present results for a given current injection as a function of the potential electrode position. The sign and magnitude of the sensitivity indicate the corresponding change in IP data following an infinitesimal change in the parameter value. This means that a model parameter changes in an area with negative sensitivity will change the datum value (the apparent resistivity or an IP gate) in the opposite way of the parameter change. The shape of the MPA sensitivity pattern is similar for all model parameters if excluding the sign, and it corresponds to the classic sensitivity pattern for a homogeneous half-space (see, e.g., Dahlin and Loke, 2015). In particular, the DC sensitivity of ρ ($\partial\rho_a/\partial\rho$) and the IP sensitivity of $\varphi_{\max}$ ($(\partial m_{a,j})/(\partial\varphi_{\max})$) for gate j) are proportional to each other, with the proportionality factor changing for the different gate index. Furthermore, note that the sign of the τ_φ-sensitivity is flipped at some point in time between gates 7 and 19. This is to be expected because a change in τ_φ will affect the magnitude of the IP gates in a different direction (an increase or decrease) depending on if the gate is in the early or late times of the IP transient.

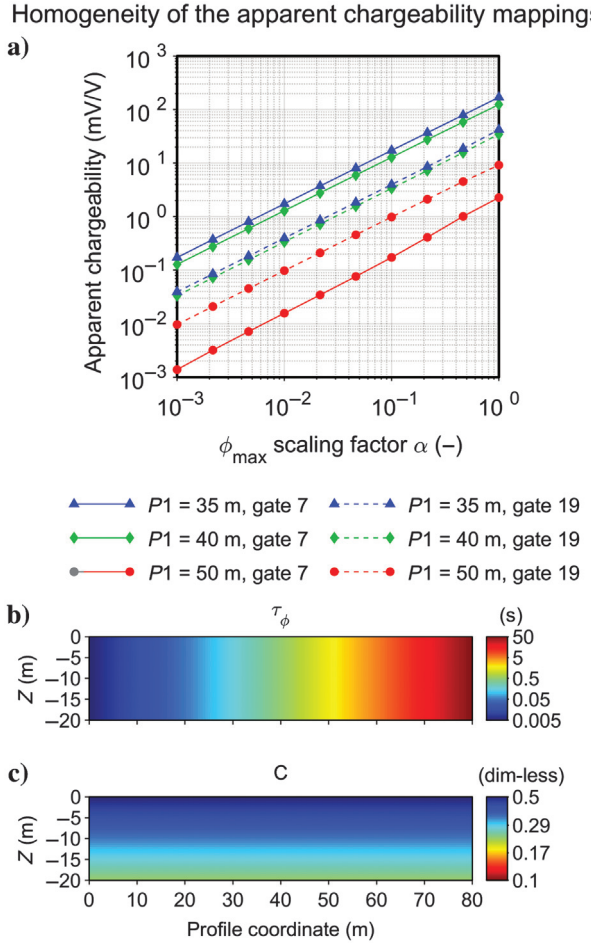

Figure 7. Apparent chargeability values as function of the $\varphi_{\max}$ scaling factor α of equation 6 (a), calculated for the τ_ϕ/C model parameters shown in (b and c) and the $\rho/\varphi_{\max}$ values depicted in Figure 6a and 6b. The blue lines and triangles: dipole-pole array with $C1$ = 25 m, $C2$ = 55 m, and $P1$ = 35 m. The green lines and diamonds: dipole-pole array with $C1$ = 25 m, $C2$ = 55 m, and $P1$ = 40 m. The red lines and circles: dipole-pole surface array with $C1$ = 25 m, $C2$ = 55 m, and $P1$ = 50 m. The continuous lines: gate 7; the dashed lines: gate 19. The flip in gates 7 and 19 magnitude for the dipole pole with $P1$ = 50 m, that the 19th gate has higher magnitude than the 7th gate, is caused by a heterodox IP transient (see Figure 8, the red markers).

The results shown in Figure 5 with proportionality between the sensitivity of ρ and $\varphi_{\max}$ for homogeneous models agree with the prediction of Seigel's approach (equation 2). To test the equivalence of Seigel's approach and our approach on heterogeneous models, we define a heterogeneous model in which ρ_0 and $\varphi_{\max}$ change with space (Figure 6, top row), but τ_φ = 0.005 s sand C = 0.5 are kept constant (to avoid a spatial variability in frequency dependence and permit a direct comparison with Seigel's approach). In particular, the heterogeneous model represents vertical variation in ρ_0 and horizontal variations in $\varphi_{\max}$. These types of parameter variations were chosen for highlighting the possible dependences of the findings on the ρ_0 and $\varphi_{\max}$ values.

Figure 6 presents, together with the ρ_0 and $\varphi_{\max}$ model, the DC ρ-sensitivity and the $\varphi_{\max}$-sensitivity (of the seventh gate), for three different dipole-pole configurations with the same current dipole ($C1$ = 25 m and $C2$ = 55 m) and different potential electrodes ($P1$ = 35, 40, and 50 m). Figure 6 also shows the ratios between the ($\rho \cdot \rho$-sensitivity), which is proportional to the chargeability sensitivity of Seigel's approach (equation 2), and the $\varphi_{\max}$-sensitivity.

The ratio plots present a strong variability vertically and horizontally, showing that the $\varphi_{\max}$ sensitivity of our approach has a dependence on the ρ_0 and $\varphi_{\max}$ parameters different from Seigel's

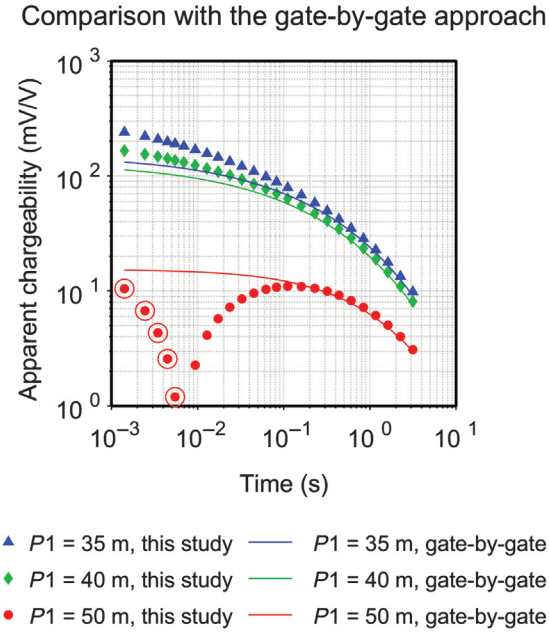

Figure 8. Comparison of the forward responses computed with the approach used in this study (the markers) and the gate-by-gate approach (the continuous lines). The model parameters used for generating the transients are depicted in Figures 6 and 7. The transients are computed for dipole-pole surface arrays with $C1$ = 25 m and $C2$ = 55 m and potential electrode: $P1$ = 35 m (the blue lines and triangles), $P1$ = 40 m (the green lines and diamonds), and $P1$ = 50 m (the red lines and circles). The circled markers represent negative data.

dependence. Similar results are obtained when using the classic resistivity Cole-Cole modeling, using m_0 instead of $\varphi_{\max}$, so these results are not a consequence of the MPA reparameterization. However, the possibility of modeling negative apparent chargeability values in Seigel's approach does not depend on the expression of the chargeability sensitivity (equation 2), but on the fact that the apparent chargeability is a homogeneous function of first degree in m and that areas of negative sensitivity exist. Consequently, we need to investigate if the apparent chargeability values $m_{a,j}$ of equation 5 are homogeneous functions of first degree in $\varphi_{\max}$, that is if the following equation holds for any positive value of the constant α:

$$f_j(\rho_0, \alpha \cdot \varphi_{\max}, \tau_\varphi, C) = \alpha \cdot f_j(\rho_0, \varphi_{\max}, \tau_\varphi, C). \quad (6)$$

The mathematical proof of equation 6 for the MPA model (or the classic Cole-Cole one) is beyond the scope of this paper, but equation 6 can easily be tested on specific models.

The equation is tested in Figure 6, on a model with the spatial variability in ρ_0 and $\varphi_{\max}$ described in Figure 6 and the spatial variability in τ_φ and C described in Figure 7 itself, which ensures a variability in the spectral content within the model. In particular, Figure 7 presents $m_{a,j} = f_j(\rho_0, \alpha \cdot \varphi_{\max}, \tau_\varphi, C)$ for α ranging from 10^{-3} to 1, for two gates (gates 7 and 19) and three dipole-pole surface arrays (with $C1$ = 25 m, $C2$ = 55 m, and different potential electrodes positions $P1$ = 35, 40, and 50 m). The maximum value

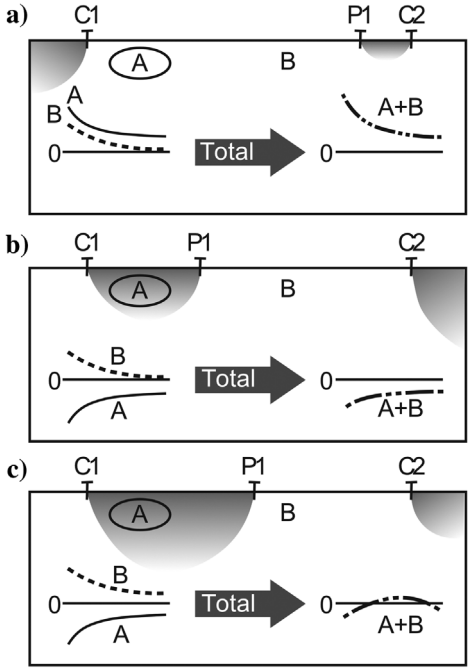

Figure 9. Illustration describing the basic mechanism for superposition of individual IP transients (from anomaly A and bulk B) and the origin of heterodox IP transients. Superpositions of contribution from positive (white) and negative (gray) sensitivity regions with different individual IP transients yield different types of total transients depending on the sensitivity pattern (electrode configuration). With the anomaly in positive sensitivity (a): type P transient. The negative sensitivity area considerably occupied by the anomaly (b): type N. The negative sensitivity area partially occupied by the anomaly (c): type NP.

$\alpha = 1$ is chosen because $\varphi_{\max}$ reaches 200 mrad in the model of Figure 4, and $\alpha > 1$ produces too-high $\varphi_{\max}$ values (equivalent to m_0 values approaching or surpassing 1000 mV/V).

Figure 7 shows that equation 6 holds, at least for the investigated model and arrays. Even if Figure 7 is not a universal proof to validate the equation, it indicates that the $m_{a,j}$ mappings are homogeneous function of first degree in $\varphi_{\max}$ to a good extent because in the used model strong parameter variations exist in all MPA parameters. However, deviations from homogeneity occur when high $\varphi_{\max}$ values exist in a large portion of the model because of the normalization with the DC potential of the apparent chargeability values (similarly to what happens in Seigel's approach through equation 1). The same approach can be used to demonstrate that the $m_{a,j}$ mappings are not homogeneous functions of the first degree in ρ_0, τ_φ, or C; analogously, in the classic Cole-Cole model the forward mappings are homogeneous functions of the first degree in m_0 to a good extent, but not in ρ_0, τ_ρ, or C (the results are not shown for brevity).

Figure 8 presents a comparison of the forward responses for the model described in Figures 6 and 7 (with $\alpha = 1$) and the same arrays of Figure 7, with the transients computed with our approach and the gate-by-gate approach of Hördt et al. (2006). The gate-by-gate computations have been carried out calculating the time-dependent resistivity values in each cell of the model discretization and using a DC forward mapping independently for each time gate. The time-dependent resistivity values are obtained through cell-by-cell time-transforming the MPA Cole-Cole dispersion, taking the current waveform into account. In Figure 8, the transients obtained with the two methods agree discretely for late times, but they consistently differ for early times. Furthermore, with the gate-by-gate approach, it is not possible to retrieve the NP transient type of the array with P = 50 m (red transients). It is worth noting that, due to the homogeneity of the apparent chargeability and apparent resistivity functions, similar results would be obtained scaling all the $\varphi_{\max}$ values by a factor α in Figure 6 — the only difference being a multiplicative factor α for all of the transients. This means that the reason for the differences is not linked to the magnitude of the IP phenomenon. In addition, the homogeneity of the apparent chargeability functions implies that not only the forward mapping but also the chargeability derivatives differ because $m_{a,j} = \sum_i \varphi_{\max,i} \cdot ((\partial f_j)/(\varphi_{\max,i}))$.

THE BASIC MECHANISM FOR HETERODOX (AND ORTHODOX) TRANSIENTS

Figure 9 shows a diagram representing the mechanisms for the generation of heterodox transients in time-domain IP data, based on data sensitivity. In the figure, a schematic sensitivity pattern is shown for three different dipole-pole IP measurements carried out on a chargeable subsurface with a homogeneous background region marked with "B" and an anomaly region marked with "A." The anomaly has a different spectral content compared to the background First, we consider the situation in which the position of the potential P1 is such that anomaly A is in an area of positive sensitivity (Figure 9a): In this case, the IP transient would be a standard type P transient. Second, when the area of negative sensitivity values is almost filled up by anomaly A (Figure 9b), the transient would be a full-negative type N transient. Finally, when the area of negative sensitivity values is only partially filled up by the anomaly

A (Figure 9c), the other types of heterodox transients might be generated (type NP, PN, ZD, or MZD).

Note the generation of heterodox IP transients without difference in φ_{max} between anomaly and background. This is shown in Figure 10, which presents the transients for dipole-pole surface arrays with a fixed current dipole ($C1$ = 25 m and $C2$ = 55 m) and various potential electrodes, for homogeneous models except for anomalies in τ_φ or C. Depending on the positions of the potential electrode, when the anomalies occupy only a portion of the areas of negative sensitivity, heterodox transients are generated (similar to Figure 9c). Sections for the heterogeneous parameters are shown in Figure 10a–10d; the parameters not shown in the figure take the values ρ_0 = 100 Ωm, φ_{max} = 5 mrad, τ_φ = 0.5 s, and C = 0.5. The middle row of the figure shows transient type pseudosections, using the position of the potential electrode P1 (of the dipole-pole array) as the pseudoposition. In the bottom row of the figure examples of transients are shown for the P1 positions highlighted by colored squares in the pseudosections. NP and PN transient types are generated when the anomaly has τ_φ values higher or lower than the surrounding medium, respectively. The ZD and MZD transient types are generated when the anomaly has C values lower than the surrounding medium, whereas NP types with multiple sign changes are generated when the anomaly has higher C values.

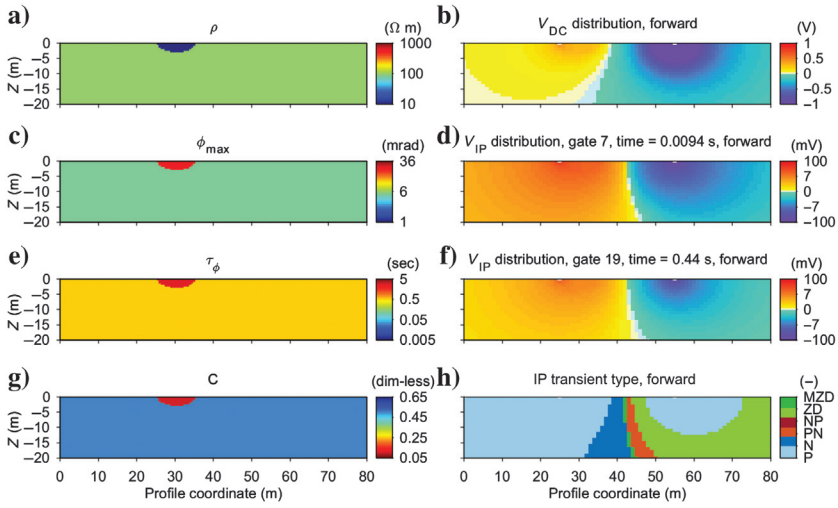

Figure 11. (a, c, e, and g) Synthetic model with a conductive chargeable anomaly (ρ_0 = 1 Ωm, φ_{max} = 25 mrad, τ_φ = 2.5 s, and C = 0.1) and a less chargeable background (ρ_0 = 100 Ωm, φ_{max} = 5 mrad, τ_φ = 0.5 s, and C = 0.5) producing multiple types of IP transients. Full model potential for (b) DC, (d and f) IP gates 7 and 19, respectively, and (h) the corresponding IP transient type. The potentials and IP transient types correspond to a current injection of 1 A with $C1$-electrode at 25 m and $C2$-electrode at 55 m.

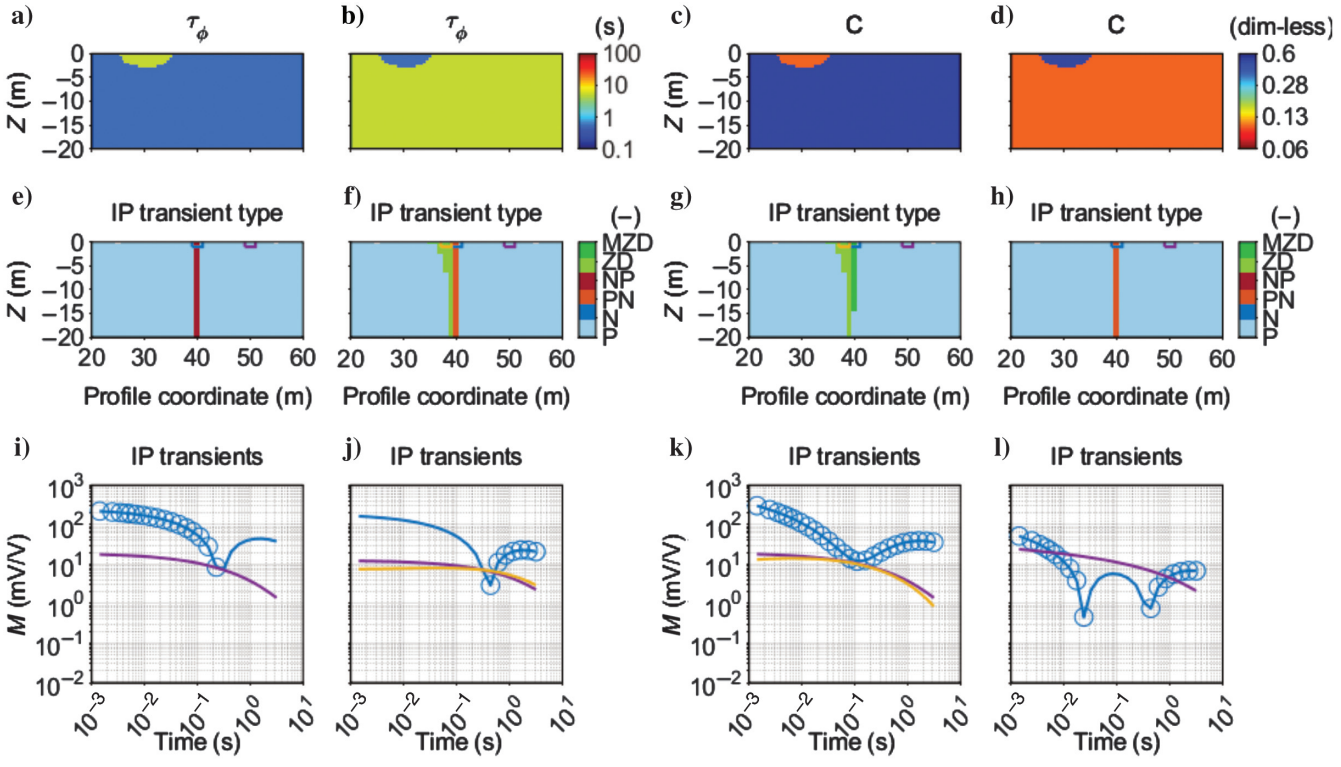

Figure 10. (a-d) Subsurface models, parameters not shown have values: ρ_0 = 10 Ωm, φ_{max} = 5 mrad, τ_φ = 0.5 s, and C = 0.5. The corresponding pseudosections (e-h) with transient types using as the position for each dipole-pole arrays the position of the potential electrode and constant current electrodes $C1$ = 25 m and $C2$ = 55 m. Exemplifying IP transients (i-l) for dipole-pole arrays marked in the pseudosection (the positions of the transients are marked with boxes of their corresponding color in the pseudosections). The circle markers indicate negative IP data.

Figure 11 shows a simple model in which all the MPA parameters change in the anomalous area (Figure 11a, 11c, 11e, and 11g), together with the sections of DC potential (Figure 11b), IP potential for selected gates (Figure 11d and 11f), and transient types (Figure 11h). For the potentials seen in Figure 11, the ratio between the IP potential and the DC potential corresponds to the IP transients expressed in mV/V. Even for this simple synthetic model, a large part of the model area has dipole-pole IP transients of multiple heterodox types (all except type NP). The heterodox transients occur at different depths, in deeper parts corresponding to the borehole measurements and, at the model surface corresponding to typical field DCIP measurements. In addition, heterodox transients can be generated for a dipole potential measurement by subtracting two pole measurements (two P1 potentials). In the examples shown so far, only 2D anomalies that produce heterodox transients have been presented, but anomalies in a 1D model space can generate any kind of heterodox types as well (Michel et al., 2020). Furthermore, similar reasoning with comparable results applies to frequency-domain responses, where the phase of the apparent complex resistivity can change the sign or present heterodox shapes, or both.

INVERSION OF FIELD DATA WITH HETERODOX TRANSIENTS

Figure 12 shows the inversion model for the field data with MPA modeling. An in-depth hydrogeologic interpretation of the inversion model is out of the scope of this paper; for detailed interpretations of DCIP measurements from the same site, though not for the same profile, the reader is referred to previous publications (e.g., Møller et al., 2016; Maurya et al., 2017, 2018). In short, the model images a groundwater plume of electrically conductive contaminants.

The data error model used in the inversion is based on the one proposed by Olsson et al. (2015) with a relative DC error of 1%, a relative IP error of 10%, and a voltage noise floor of 0.5 mV for a nominal integration time of 0.01 s and one stack. Recognizing that by definition these transients have a magnitude of zero mV/V at some point in time, and are thus especially sensitive to measurement noise, the noise model was modified to take this into account. Specifically, the extra relative error is added for the negative gate closest to a zero passing and its adjacent gates (type PN and NP). For these gates, the extra error ($\mathrm{STD_{ZP}}$) is computed as $\mathrm{STD_{ZP}}(k \pm i) = 1/3^i$, where k is the index of the negative gate closest to the zero passing and i is a positive integer ranging from 0 to 2. Thus, with this computation, five gates will get an increased error, the gate index k, which is close to the zero passing, will get the largest error, and its two closest adjacent gates will get a smaller error, whereas the next two gates further from the index k get the smallest error addition.

Figure 13 shows pseudosections for the forward response of the inversion model in terms of negative or positive apparent integral chargeability and IP transient types with all of the standard and heterodox types represented. Regions with a negative and higher magnitude of apparent integral chargeability in the field data are well reproduced by the forward response (Figure 13). In addition, the major patterns in the IP transient type pseudosection are captured down to approximately 25 m in pseudodepth.

At greater pseudodepths, almost all forward IP transients are of type P, even though there are multiple heterodox types in the data. It is not clear why this mismatch between IP transient types at depth is present, but it can be an effect of increased inductive and capacitive coupling

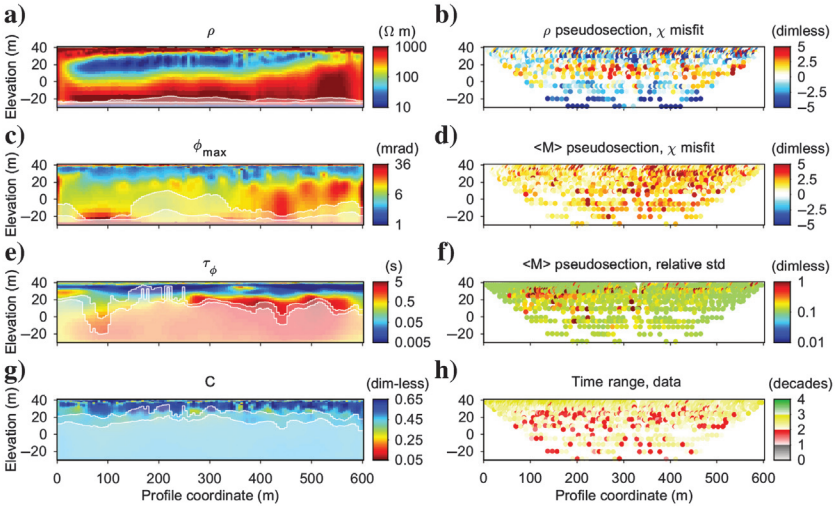

Figure 12. Inversion model for (a, c, e, and g) the field data inversion, (b and d) inversion χ-misfit, (f) mean IP transient STD, and (h) after-processing data time range.

Table 2. Summary of the number of transients in the field and forward data corresponding to each IP transient type and their corresponding match.

IP transient type	P	N	PN	NP	ZD	MZD	Total
Number of transients in the field data (—)	858	399	39	202	105	18	1621
Percent of transients in the field data (%)	52.9	24.6	2.4	12.5	6.5	1.1	100
Number of transients in the forward data (—)	1007	393	15	110	70	26	1621
Percent of transients in the forward data (%)	62.1	24.2	0.9	6.8	4.3	1.6	99.9
Number of transients matching type (—)	830	370	10	83	17	9	1319
Percent of transients matching type (%)	96.7	92.7	25.6	41.1	16.2	50	81.4

effects for the larger electrode spacing used for measurements corresponding to larger pseudodepths. It could also be caused by the coarser model discretization at depth so that no model, which can reproduce heterodox transient, can be constructed or by a general loss of resolution with depth.

In either case, our handling of coupling effects needs to be developed in the future so they can be differentiated or canceled from the potential transient, and inversion routines need to be improved for facilitating the inversion of heterodox IP transients. Furthermore, semi- or fully automated data processing schemes need to be designed with care and with conservative assumptions regarding the allowed shapes of IP transients so that heterodox transients are not routinely removed from the data sets. For the inversion presented in this paper, the final χ-misfits are 2.8 and 2.4 for DC and IP, respectively. The high value for the DC χ-misfit is not particularly significant. Indeed, the small value for the DC error (1%) was chosen to balance the relative weight of DC and IP data in the objective function, and not because DC data are expected to be accurate within 1%. The high value for the IP χ-misfit arises from a nonperfect match between the measured and forward response types, as described previously for the deeper pseudodepths.

A summary of the number of the IP transients in the forward data corresponding to each IP transient type, as well as the percentage, is provided in Table 2. Approximately 38% of the IP forward data consist of heterodox transient types. Clearly, the previously discarded heterodox IP transients can be modeled and should be considered for being included in the inversion. Consequently, there is a need for reconsidering semiautomated data processing for rejecting data based on the assumption of standard type P transients (e.g., Flores Orozco et al., 2018).

Figure 14 shows the field IP transients from Figure 1 together with their corresponding forward responses. It is evident that the forward responses of the inversion model can reproduce all standard and heterodox IP transient types present in the field data, to a large extent also within the estimated error bars.

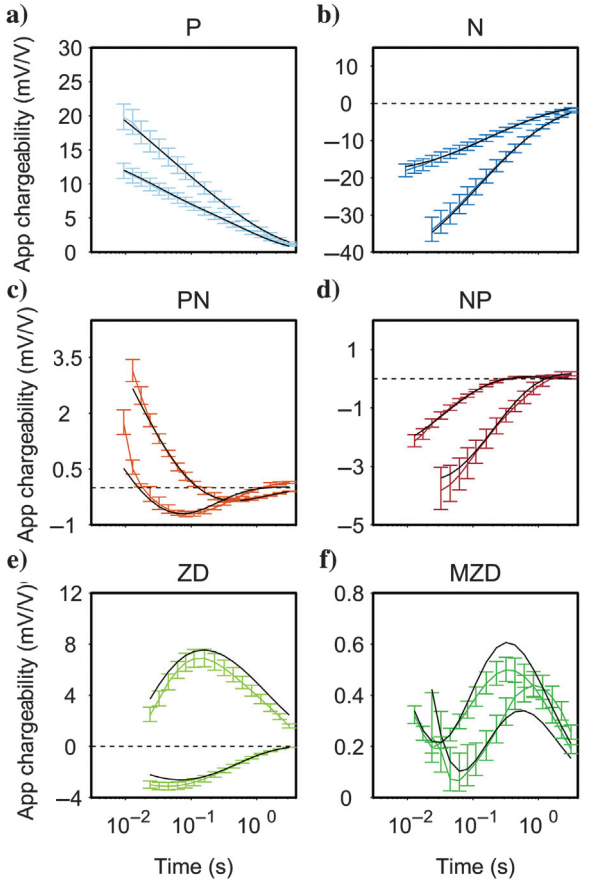

Figure 14. (a-f) Example of individual IP transients in the forward data (black) and their corresponding field data with error bars. The focus positions of the example transients are marked in Figures 2a and 2b and 13a and 13b. Note that the apparent chargeability ranges differ between the panels.

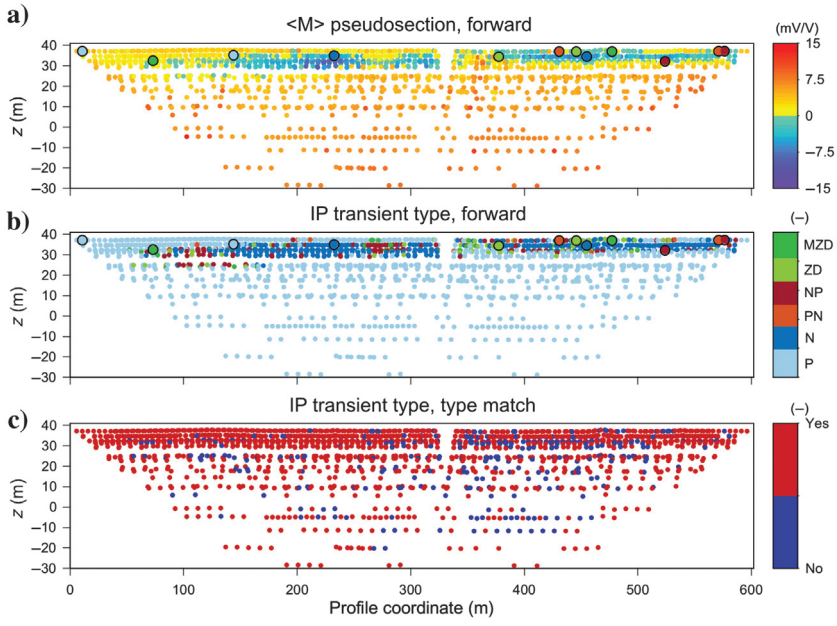

Figure 13. (a) Pseudosections showing apparent integral chargeability, (b) IP transient type for the forward data set of the inversion model, and (c) the type match between the forward response and the field data. The colored circles with the black outline mark the positions of the example transients shown in Figures 1 and 14.

CONCLUSION

IP transients with heterodox relaxation shapes such as a negative or zero-passing amplitude, or ZD can represent correct measurements and should not routinely be considered as outliers caused by measurement noise. Such transients have been proven to be possible by field measurements, synthetic numerical modeling, and inversion of field data, and a theoretical explanation has been given for the basic mechanism of their origin. Furthermore, the processing of full-waveform signals allows for evaluating the quality of the background removal process, and to reject possibly erroneous, heterodox transients. The accuracy and reliability of inversion models can be increased by including also heterodox IP transients because more information is used to produce the subsurface models. However, the signal levels of many heterodox types are often small (e.g., type PN, NP) and care needs to be taken to minimize problems with data quality and reliability. The increased understanding of IP transients in general and the introduced classification system could serve as the first steps toward automated processing of full-transient IP data that could help in distinguishing reasonable IP transients from those with poor data quality. Actually, this reoccurrence of heterodox transients on several profiles triggered our attention to the possibility that the transients were correct.

However, in general, it is a challenging task to deal with heterodox IP transient types and care needs to be taken in all steps involved in acquiring subsurface DCIP information. Survey procedures and data processing need to be thoroughly done to ensure that the data are reliable, and inversion settings might need to be tuned to get a decent data fit. Hence, it is relevant to systematically reassure that appropriate measures have been taken, as outlined in this paper, before accepting heterodox transients. Moreover, additional research is needed for improving our practice in these steps.

ACKNOWLEDGEMENTS

Funding for the work was provided by Formas — The Swedish Research Council for Environment, Agricultural Sciences and Spatial Planning (ref. 2012-1931), BeFo — Swedish Rock Engineering Research Foundation (ref. 331), and SBUF — The Development Fund of the Swedish Construction Industry (ref. 13232). The project is part of the Geoinfra-TRUST framework (http://trust-geoinfra.se/). The Innovation Fund Denmark provided additional funding via the GEOCON project (http://www.geocon.env.dtu.dk/). Furthermore, the work is jointly funded by the European Union, Eurostars Programme, Central Region Denmark, Innovation Fund Denmark, and The Swedish innovation agency Vinnova under the project "Mapping Geology in Cities" (E10096 MAGIC).

DATA AND MATERIALS AVAILABILITY

The software Aarhusinv is freely distributed for research purposes. Details on how to obtain code and license are found at https://hgg.au.dk/software/aarhusinv/.

REFERENCES

Bertin, J., and J. Loeb, 1976, Experimental and theoretical aspects of induced polarization, *in* R. G. van Nostrand and S. Saxov, eds., Macroscopic and Microscopic Theories, **2**, Schweizerbart Science Publishers.

Chartrand, R., 2011, Numerical differentiation of noisy, nonsmooth data: ISRN Applied Mathematics, **2011**, 1–11, doi: 10.5402/2011/164564.

Cole, K. S., and R. H. Cole, 1941, Dispersion and absorption in dielectrics — 1: Alternating current characteristics: The Journal of Chemical Physics, **9**, 341, doi: 10.1063/1.1750906.

Dahlin, T., V. Leroux, and J. Nissen, 2002, Measuring techniques in induced polarisation imaging: Journal of Applied Geophysics, **50**, 279–298, doi: 10.1016/S0926-9851(02)00148-9.

Dahlin, T., and M. H. Loke, 2015, Negative apparent chargeability in time-domain induced polarisation data: Journal of Applied Geophysics, **123**, 322–332, doi: 10.1016/j.jappgeo.2015.08.012.

Doetsch, J., G. Fiandaca, E. Auken, A. V. Christiansen, A. G. Cahill, and R. Jakobsen, 2015a, Field-scale time-domain spectral induced polarization monitoring of geochemical changes induced by injected CO_2 in a shallow aquifer: Geophysics, **80**, no. 2, WA113–WA126, doi: 10.1190/geo2014-0315.1.

Doetsch, J., T. Ingeman-Nielsen, A. V. Christiansen, G. Fiandaca, E. Auken, B. Elberling, K. Adamson, T. Lane, and B. Elberling, 2015b, Direct current (DC) resistivity and induced polarization (IP) monitoring of active layer dynamics at high temporal resolution: Cold Regions Science and Technology, **119**, 16–28, doi: 10.1016/j.coldregions.2015.07.002.

Fiandaca, G., E. Auken, A. V. Christiansen, and A. Gazoty, 2012, Time-domain-induced polarization: Full-decay forward modeling and 1D laterally constrained inversion of Cole-Cole parameters: Geophysics, **77**, no. 3, E213–E225, doi: 10.1190/geo2011-0217.1.

Fiandaca, G., J. Doetsch, G. Vignoli, and E. Auken, 2015, Generalized focusing of time-lapse changes with applications to direct current and time-domain induced polarization inversions: Geophysical Journal International, **203**, 1101–1112, doi: 10.1093/gji/ggv350.

Fiandaca, G., P. K. Maurya, N. Balbarini, A. Hördt, A. V. Christiansen, N. Foged, P. L. Bjerg, and E. Auken, 2018, Permeability estimation directly from logging-while-drilling induced polarization data: Water Resources Research, **54**, 2851–2870, doi: 10.1002/2017WR022411.

Fiandaca, G., J. Ramm, A. Binley, A. Gazoty, A. V. Christiansen, and E. Auken, 2013, Resolving spectral information from time domain induced polarization data through 2-D inversion: Geophysical Journal International, **192**, 631–646, doi: 10.1093/gji/ggs060.

Flores Orozco, A., J. Gallistl, M. Bücker, and K. H. Williams, 2018, Decay curve analysis for data error quantification in time-domain induced polarization imaging: Geophysics, **83**, no. 2, E75–E86, doi: 10.1190/geo2016-0714.1.

Gazoty, A., G. Fiandaca, J. Pedersen, E. Auken, and A. V. Christiansen, 2012a, Mapping of landfills using time-domain spectral induced polarization data: The Eskelund case study: Near Surface Geophysics, **10**, 575–586, doi: 10.3997/1873-0604.2012046.

Gazoty, A., G. Fiandaca, J. Pedersen, E. Auken, A. V. Christiansen, and J. K. Pedersen, 2012b, Application of time domain induced polarization to the mapping of lithotypes in a landfill site: Hydrology and Earth System Sciences, **16**, 1793–1804, doi: 10.5194/hess-16-1793-2012.

Hönig, M., and B. Tezkan, 2007, 1D and 2D Cole-Cole-inversion of time-domain induced-polarization data: Geophysical Prospecting, **55**, 117–133, doi: 10.1111/j.1365-2478.2006.00570.x.

Hördt, A., T. Hanstein, M. Hönig, and F. M. Neubauer, 2006, Efficient spectral IP-modelling in the time domain: Journal of Applied Geophysics, **59**, 152–161, doi: 10.1016/j.jappgeo.2005.09.003.

Ingeman-Nielsen, T., S. Tomaškovičová, and T. Dahlin, 2016, Effect of electrode shape on grounding resistances — Part 1: The focus-one protocol: Geophysics, **81**, no. 1, WA159–WA167, doi: 10.1190/geo2015-0484.1.

Johansson, S., G. Fiandaca, and T. Dahlin, 2015, Influence of non-aqueous phase liquid configuration on induced polarization parameters: Conceptual models applied to a time-domain field case study: Journal of Applied Geophysics, **123**, 295–309, doi: 10.1016/j.jappgeo.2015.08.010.

Johansson, S., C. Sparrenbom, G. Fiandaca, A. Lindskog, P.-I. Olsson, T. Dahlin, and H. Rosqvist, 2017, Investigations of a Cretaceous limestone with spectral induced polarization and scanning electron microscopy: Geophysical Journal International, **208**, 954–972, doi: 10.1093/gji/ggw432.

Jung, H.-K., D.-J. Min, H. S. Lee, S. Oh, and H. Chung, 2009, Negative apparent resistivity in dipole–dipole electrical surveys: Exploration Geophysics, **40**, 33–40, doi: 10.1071/EG08111.

Kang, S., and D. W. Oldenburg, 2018, Time domain electromagnetic-induced polarisation: Extracting more induced polarisation information from grounded source time domain electromagnetic data: Geophysical Prospecting, **66**, 74–86, doi: 10.1111/1365-2478.12600.

Kemna, A., 2000, Tomographic inversion of complex resistivity: Theory and application: Der Andere Verlag.

Loeb, J., and J. Bertin, 1976, Experimental and theoretical aspects of induced polarization, *in* R. G. van Nostrand and S. Saxov, eds., Presentation and Application of the IP Method Case Histories, **1**, Schweizerbart Science Publishers.

Madsen, L. M., G. Fiandaca, E. Auken, and A. V. Christiansen, 2017, Time-domain induced polarization — An analysis of Cole–Cole parameter resolution and correlation using Markov Chain Monte Carlo inversion: Geophysical Journal International, **211**, 1341–1353, doi: 10.1093/gji/ggx355.

Maurya, P. K., N. Balbarini, I. Møller, V. Rønde, A. V. Christiansen, P. L. Bjerg, E. Auken, and G. Fiandaca, 2018, Subsurface imaging of water electrical conductivity, hydraulic permeability and lithology at contaminated sites by induced polarization: Geophysical Journal International, **213**, 770–785, doi: 10.1093/gji/ggy018.

Maurya, P. K., V. K. Rønde, G. Fiandaca, N. Balbarini, E. Auken, P. L. Bjerg, and A. V. Christiansen, 2017, Detailed landfill leachate plume mapping using 2D and 3D electrical resistivity tomography — With correlation to ionic strength measured in screens: Journal of Applied Geophysics, **138**, 1–8, doi: 10.1016/j.jappgeo.2017.01.019.

Michel, H., F. Nguyen, T. Kremer, A. Elen, and T. Hermans, 2020, 1D geological imaging of the subsurface from geophysical data with Bayesian evidential learning: Computers and Geosciences, **138**, 104456, doi: 10.1016/j.cageo.2020.104456.

Møller, I., P. K. Maurya, N. Balbarini, G. Fiandaca, A. V. Christiansen, H. Holm, V. K. Rønde, K. E. S. Klint, E. Auken, and P. L. Bjerg, 2016, Is the IP response related to geology or contaminants in a leachate plume at the Grindsted Landfill, Denmark?: Proceedings of the 4th International Workshop on Induced Polarization, 1–3.

Olsson, P.-I., T. Dahlin, G. Fiandaca, and E. Auken, 2015, Measuring time-domain spectral induced polarization in the on-time: Decreasing acquisition time and increasing signal-to-noise ratio: Journal of Applied Geophysics, **123**, 316–321, doi: 10.1016/j.jappgeo.2015.08.009.

Olsson, P.-I., G. Fiandaca, J. J. Larsen, T. Dahlin, and E. Auken, 2016, Doubling the spectrum of time-domain induced polarization by harmonic denoising, drift correction, spike removal, tapered gating and data uncertainty estimation: Geophysical Journal International, **207**, 774–784, doi: 10.1093/gji/ggw260.

Pelton, W. H., S. H. Ward, P. G. Hallof, W. R. Sill, and P. H. Nelson, 1978, Mineral discrimination and removal of inductive coupling with multifrequency IP: Geophysics, **43**, 588–609, doi: 10.1190/1.1440839.

Rossi, M., P.-I. Olsson, S. Johansson, G. Fiandaca, D. Preis Bergdahl, and T. Dahlin, 2017, Mapping geological structures in bedrock via large-scale direct current resistivity and time-domain induced polarization tomography: Near Surface Geophysics, **15**, 657–667, doi: 10.3997/1873-0604.2017058.

Seigel, H. O., 1959, Mathematical formulation and type curves for induced polarization: Geophysics, **24**, 547–565, doi: 10.1190/1.1438625.

Spiegel, M. R., 1974, Schaum's outline of theory and problems of advanced calculus, SI metric: McGraw-Hill book Company.

Sumner, J. S., 1976, Principles of induced polarization for geophysical exploration: Elsevier.

Van Voorhis, G. D., P. H. Nelson, and T. L. Drake, 1973, Complex resistivity spectra of porphyry copper mineralization: Geophysics, **38**, 49–60, doi: 10.1190/1.1440333.

Wang, C., A. Binley, and L. D. Slater, 2021, On negative induced polarization in frequency domain measurements: Geophysical Journal International, **225**, 342–353, doi: 10.1093/gji/ggaa581.

Wemegah, D. D., G. Fiandaca, E. Auken, A. Menyeh, and S. K. Danuor, 2017, Spectral time-domain induced polarisation and magnetic surveying — An efficient tool for characterisation of solid waste deposits in developing countries: Near Surface Geophysics, **15**, 75–84, doi: 10.3997/1873-0604.2016048.

Yuval and Oldenburg, D. W., 1997, Computation of cole-cole parameters from IP data: Geophysics, **62**, 1419–1431, doi: 10.1190/1.1444154.

Biographies and photographs of the authors are not available.